Re-analysis of the Cassini RPWS/LP data in Titan's ionosphere. Part I: detection of several electron populations

Audrey Chatain, J.-E. Wahlund, O. Shebanits, L. Z. Hadid, M. Morooka, N. J. T. Edberg, O. Guaitella, Nathalie Carrasco

HAL Id: insu-03298835
https://insu.hal.science/insu-03298835

Submitted on 26 Jul 2021

1   **Re-analysis of the Cassini RPWS/LP data in Titan's ionosphere. Part I: detection of**
2   **several electron populations**

3

4   **A. Chatain[1,2], J.-E. Wahlund[3], O. Shebanits[3,4], L. Z. Hadid[2,3], M. Morooka[3], N. J. T. Edberg[3],**
5   **O. Guaitella[2], and N. Carrasco[1]**

6   [1] Université Paris-Saclay, UVSQ, CNRS, LATMOS, Guyancourt, France.

7   [2] LPP, Ecole polytechnique, Sorbonne Université, Institut Polytechnique de Paris, CNRS,
8   Palaiseau, France.

9   [3] Swedish Institute of Space Physics, Uppsala, Sweden.

10   [4] Imperial College London, United-Kingdom.

11

12   Corresponding author: Audrey Chatain (audrey.chatain@ens-paris-saclay.fr)

13

14   **Key Points:**

15   • The Cassini Langmuir probe dataset in Titan's ionosphere is re-analyzed with a specific
16   interest on the electron density and temperature.

17   • 2 to 4 cold electron populations with distinct potentials are observed.

18   • Electron populations vary with altitude and solar illumination suggesting origins linked to
19   solar photons, magnetospheric particles and dust

20

21

22 **Abstract**

23 Current models of Titan's ionosphere have difficulties in explaining the observed electron density
24 and/or temperature. In order to get new insights, we re-analyzed the data taken in the ionosphere
25 of Titan by the Cassini Langmuir probe (LP), part of the Radio and Plasma Wave Science (RPWS)
26 instrument. This is the first of two papers that present the new analysis method (current paper) and
27 statistics on the whole dataset. We suggest that between 2 and 4 electron populations are necessary
28 to fit the data. Each population is defined by a potential, an electron density and an electron
29 temperature and is easily visualized by a dinstinct peak in the second derivative of the electron
30 current, which is physically related to the electron energy distribution function (Druyvesteyn
31 method). The detected populations vary with solar illumination and altitude. We suggest that the
32 4 electron populations are due to photo-ionization, magnetospheric particles, dusty plasma and
33 electron emission from the probe boom, respectively.

34

1 Introduction

36 The Cassini mission explored the Saturnian system from 2004 to 2017 and gave us unprecedented
37 insights on the ionosphere of Titan, the biggest moon of Saturn (Coates et al., 2007; Wahlund et
38 al., 2005; Waite et al., 2005). This ionized environment hosts a complex ion chemistry that leads
39 to the formation of organic aerosols (Vuitton et al., 2019; Waite et al., 2007). The Cassini mission
40 investigated Titan at the occasion of 126 close flybys, and probed the ionosphere below the altitude
41 of 1200 km for 57 of these flybys. There is a substantial coverage of measurements taken at
42 different solar zenith angles, latitudes and seasons, enabling statistical analyses.

43 The study here is focused on electrons in Titan's ionosphere. The electron density was previously
44 observed to be mainly governed by solar photons during the day (Ågren et al., 2009).
45 Photoionization of the neutral molecules lead to a maximum electron density ($\sim$2000 cm^{-3}) around
46 1100 km altitude. The electron density have also been observed to vary (up to factor 2 at the peak)
47 with the solar cycle (Edberg et al., 2013). On the nightside, electron transport from the dayside
48 and the thermalization of magnetospheric electrons give a constant electron density of $\sim$400-700
49 cm^{-3} from 1200 km to < 950 km (Ågren et al., 2009; Cravens et al., 2009; Cui et al., 2009; Shebanits
50 et al., 2017b).

51 Below 1100 km of altitude, positive, negative ions and dust have increasing densities, and start to
52 affect the electrons (Shebanits et al., 2013, 2016; Waite et al., 2007). In particular, dust particles
53 in a dense ionized environment tend to attract electrons and charge negatively (e.g. Farrell et al.,
54 2009; Shukla & Mamun, 2015). It explains whay the electron density decreases below 1100 km,
55 while the density of ions and negatively charged dust increase and become the dominant negative
56 charge carriers (e.g. Shebanits et al., 2013, 2016).

57 The temperature of the bulk electrons can be deduced from measurements by the Langmuir probe
58 on-board Cassini. Ågren et al. (2009) and Edberg et al. (2010) derived the electron temperature
59 profiles (assuming a single Maxwellian electron distribution) from 52 flybys down to $\sim$900 km of
60 altitude and stated a rather stabilized temperature below 1100 km. The observed values ranged
61 from 0.03 to 0.06 eV ($\approx$ 350-700 K).

62 Several models have been developed to understand the processes at work in Titan's ionosphere
63 (e.g. Galand et al., 2014 and references therein). Nevertheless, model results either predict too cold

64 electrons (< 0.02 eV; < 200 K) at 900 km (Mukundan & Bhardwaj, 2018; Richard et al., 2011) or
65 an overestimated electron density by a factor of 2 (Vigren et al., 2013, 2016). The addition of the
66 negative ions to a photoionisatoin model has been shown to decrease the discrepancy with the
67 measurements (Shebanits et al., 2017a).

68 The present work aims to closely investigate the measurements of the electron density and
69 temperature in the ionosphere of Titan, focusing on the interaction between electrons and negative
70 ions and dust. For this purpose, we re-analyzed the measurements acquired by the Langmuir probe
71 (LP) part of the Radio and Plasma Wave Science (RPWS) investigation on-board Cassini, during
72 the 13 years of the mission. This work is presented in two parts. In a first paper (this one), we detail
73 the method used for the re-analysis of the data and the detection of several electron populations.
74 A second paper (Chatain et al., n.d.), referred as 'paper II', presents the results obtained for 57
75 flybys and discusses the origins of the detected electron populations.

76

2 Methods

2.1 Langmuir Probe measurements

79 The Langmuir probe on-board Cassini was built by the Swedish Institute of Space Physics (IRF).
80 It was positioned below the radio antenna, on a 1.5 m boom to minimize electric perturbation from
81 the spacecraft (Gurnett et al., 2004). The probe was a sphere of titanium of 5 cm in diameter, coated
82 with titanium nitride, chosen foremost for its electrical work function stability, chemical inertness,
83 high reflectivity and limited photoelectric effects. It is also very hard, enhancing solid particle
84 impact resistance and eliminating hysteresis effects that are observed with other surface coatings
85 (Wahlström et al., 1992). A small part of the stick (the stub) closest to the sphere was kept at the
86 probe potential to ensure a symmetric potential pattern and sampling around a swept probe. A
87 cleaning mode enabled to remove a possible contamination on the surface. In this mode, the
88 potential of the sphere was set at +32 V to induce sputtering of the probe with high energy
89 electrons.

90 In this study, we used the measurements from the sweep mode of the probe. The current collected
91 by the probe during the voltage sweep enables to deduce the electron density and temperature
92 (among other useful derived parameters of interest). On Titan, the probe usually acquired double-
93 sweeps, in 512 x2 voltage steps, from +4 V to -4 V, and back to +4 V, to give an idea of possible
94 surface contamination effects. In addition, to detect any charging effects, for both of the sweeps
95 the current was measured twice at each voltage step.

96 In this work, we first investigated the reproducibility of the measurements with the two voltage
97 sweeps (named 'down' and 'up'), and the double measurements at each voltage step (resp.
98 'down1'-'down2' and 'up1'-'up2'). We observed that 'down1' and 'down2' are always very close
99 to each other: the current stabilizes quickly after each voltage step. However, during the increasing
100 voltage phase ('up1'and 'up2'), the current continues to increase sligthly between the two
101 measurements. Further details are given in Appendix A.

102 In the following, we did not take the average of 'down' and 'up' because in some cases a shift in
103 the measured plasma potential between both would distort the average signal. We generally used
104 the average of the decreasing part of the sweep ('down'). Nevertheless, we used also the average
105 of 'up1' and 'up2' in the few cases where the decreasing part of the sweep was not acquired. We

106   analyzed the impact of using the 'down' or the 'up' signal in our study and concluded that this
107   effect was negligible compared to the fit error bars (see further). An example is given in Supporting
108   Information Figure S1.

109

110   2.2 Theory to fit the electron and positive ion current

111   The Orbital Motion Limited (OML) theory is used to fit the voltage sweeps measured by the
112   Langmuir probe. A correction is added in the attractive bias voltage region using the Sheath
113   Limited theory (SL).

114   The OML theory, first described by Mott-Smith & Langmuir (1926), deduces information on the
115   charged particles from the current measured by the probe, based on the conservation of energy and
116   angular momentum. No particle is assumed to come from the probe itself and the bulk particle
117   speed distribution is assumed Maxwellian. The OML theory is valid when the probe radius is
118   smaller than the Debye length in the probed region. In these conditions, the electron and ion
119   currents (respectively I_e and I_i) are described by two different equations depending on the sign of
120     $\Delta U = U_{bias} - U_P$ (Wahlund et al., 2009; Whipple, 1965), U_{bias} being the potential of the probe
121   and U_P the characteristic potential of the electron/ion population in the plasma. The electron
122   current I_e (resp. the ion current I_i) is expressed as a function of $I_{e,0}$ (or $I_{i,0}$) and χ_e (resp. χ_i):

$$I_x = I_{x,0}\,(1 - \chi_x)$$

$$x = e \text{ if } \Delta U > 0, x = i \text{ if } \Delta U < 0$$
$$[\text{'attractive' part for electrons}]$$
(1)

$$I_x = I_{x,0}\,\exp(-\chi_x)$$

$$x = e \text{ if } \Delta U < 0, x = i \text{ if } \Delta U > 0$$
$$[\text{'repelling' part for electrons}]$$
(2)

123   The two equations join in $\Delta U = 0$. Then, the collected current $I_{x,0}$ is formulated as follows. It
124   combines the effect of flow kinetic energy and thermal energy (Fahleson et al., 1974):

$$I_{x,0} = -A_{LP}.n_x.q_x.\sqrt{\frac{v_x^2}{16} + \frac{k_B T_x}{2\pi.m_x}}$$
(3)

125   A_{LP} is the surface area of the probe. n_x, q_x, v_x, T_x and m_x are respectively the density, charge,
126   velocity, temperature and mass of electrons or ions, and k_B is the Boltzmann constant.

127   The parameter χ_x depends on ΔU and is expressed as:

$$\chi_x = \frac{q_x.\Delta U}{\frac{m_x v_x^2}{2} + k_B T_x}$$
(4)

128   In the case of electrons, the flow kinetic energy term can be neglected compared to the thermal
129   term. It is the opposite in the case of ions (positive and negative), which are heavier than electrons
130   and transported along the ion ram flux. When $\Delta U \ll 0$, the collected current is governed by
131   positive ions while it is dominated by electrons when $\Delta U > 0$.

132

133 In Titan's ionosphere, the Debye length ($\lambda_D \approx 2.5 - 10.5\ cm$) is similar to the radius of the probe
134 ($r_p = 2.5\ cm$). It is the limit of validity to use the OML theory. Therefore, a small correction is
135 added by using the Sheath Limited (SL) theory (Bettinger & Walker, 1965; Whipple, 1965), valid
136 in a collisionless maxwellian plasma. It adds the dependence of the sheath thickness (s) with the
137 potential and size of the probe and changes the expression of the attractive part. For electrons, it
138 gives for $\Delta U > 0$:

$$I_e = I_{e,0} \times \left[1 + \xi \times \left(1 - \exp\left(-\frac{\chi_e}{\xi} \right) \right) \right]$$

$$\text{with}\ \ \xi = \left(\frac{s}{\rho} + 1 \right)^2 - 1, \qquad \rho = \frac{r_p}{\lambda_D} \tag{5}$$

$$\text{and}\ \ \ s = 0.83 \cdot \sqrt{\chi_e} \cdot \rho^{\frac{1}{3}}$$

139 The expression of the sheath thickness (s) is empirically obtained by Bettinger and Walker (1965)
140 in the case of spherical bodies. These expressions converge to the OML expressions when $s \gg r_p$.

141

142 The electron temperature and the Electron Energy Distribution Function (EEDF) can be obtained
143 from the 'transition region', the part of the voltage sweep where the electron current starts to
144 dominate the positive ion current, i.e. for ΔU being slightly negative (of a few tenths of volts in
145 the conditions of Titan's ionosphere).

146 In this transition region, the positive ion current is not always negligible compared to the electron
147 current. To obtain the electron current, the measured (total) current is therefore corrected from the
148 positive ion part, fitted by a linear curve (see Equation (1)). An example is given in Supporting
149 Information Figure S2.

150

151 　　　2.3 Example of electron current collected in Titan's ionosphere: observation of several
152 　　　electron populations

153 The electron part is fitted with Equations (2) and (5). Nevertheless, using only one electron
154 'population' (i.e. one combination of Equations (2) and (5)) results in a poor fit of the electron
155 current collected in the ionosphere. Generally, a second population has to be added. It leads to two
156 different sets of (U_P, n_e, T_e). An example is shown in Figure 1.

157 Below 1300 km, two maxwellian populations of electrons are often still not sufficient to correctly
158 fit the electron current. A third, and in rare occasions a fourth, population is required. An example
159 with three populations is shown in Figure 2 and examples with one and four populations are given
160 in Supporting Information Figure S3 and S4. In conclusion, the analysis of voltage sweeps in the
161 ionosphere of Titan often leads to 2-4 sets of (U_P, n_e, T_e) per sweep. The fitting procedure is
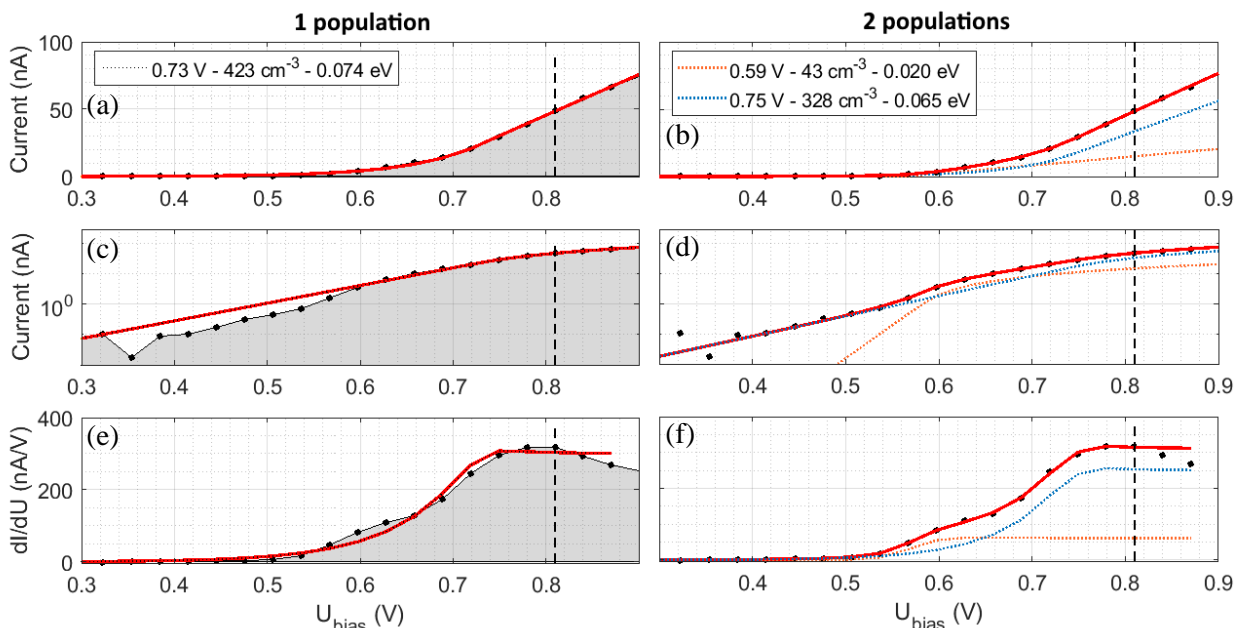162 detailed in Appendix B.

163

164

Figure 1. Fitting of the voltage sweep acquired during T50 at 1241 km altitude. (a,c,e) One electron
population is used for fitting. (b,d,f) Two electron populations are used for fitting. The fit results (U_p, n_e, T_e)
for each population are indicated on the graphs. The part of the curves after the dashed line corresponds to
a part possibly distorted by the effect of a logarithmic pre-amplifier, and should not be used without further
consideration.

170

Figure 2. Fitting of the voltage sweep acquired during T50 at 1125 km altitude. (a,c,e) Two electron
populations are used for fitting. (b,d,f) Three electron populations are used for fitting. The fit results
(U_p, n_e, T_e) for each population are indicated on the graphs. The part of the curves after the dashed line
corresponds to a part possibly distorted by the effect of a logarithmic pre-amplifier, and should not be used
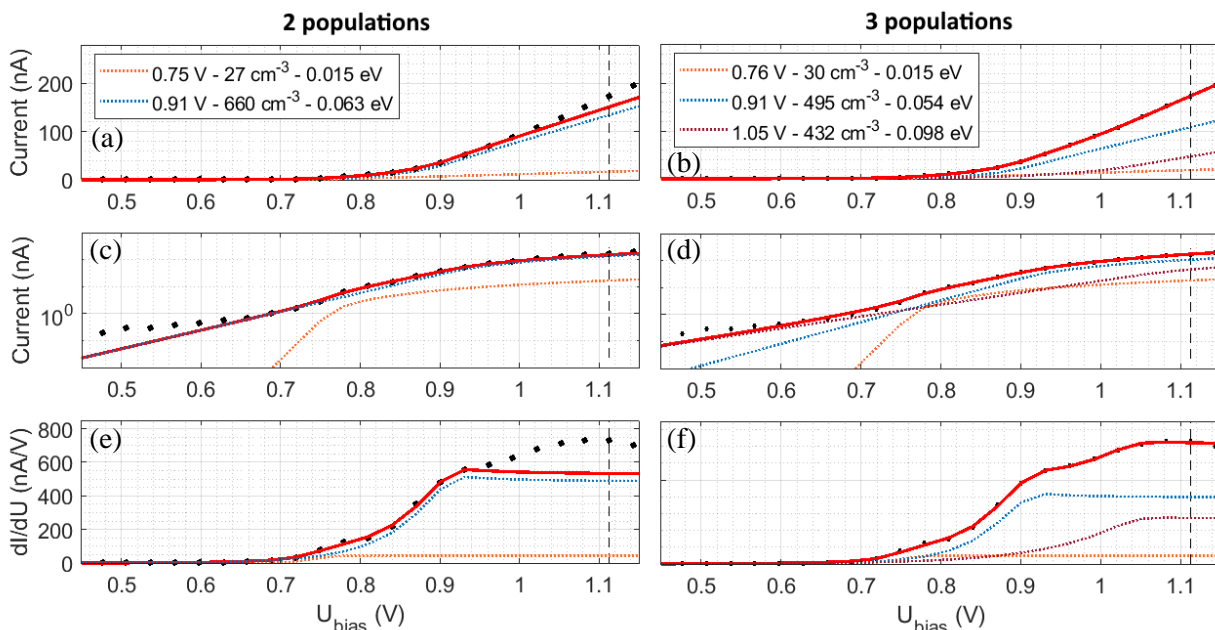without further consideration.

176

177   2.4 The second derivative of the electron current (d²I/dU²): an effective method to detect
178   the electron populations

179 The second derivative of the current is a good indicator of the presence of several electron
180 populations. Each peak corresponds to a population, and its area is globally proportional to the
181 electron density associated (this is explained in Section 2.5). Figure 3 shows d²I/dU² associated
182 with the fitted sweeps plotted in Figure 1 and 2. Cases with 1 and 4 populations are shown in
183 Supporting Information Figure S5.

184 The data points are at very low resolution, with only four to ten points per peak. Consequently, the
185 computation of the second derivative is strongly impacted. This effect is illustrated in Figure 3:
186 the red curve shows d²I/dU² computed from the fit with the (low) resolution of the data points, and
187 the orange dotted-dashed line gives d²I/dU² with a high resolution (with >200 points per peak).

188 The confidence intervals on the fit results (U_P, n_e, T_e) for all the populations are also computed
189 (see details in Appendix C) and are plotted in the Figures of section 3.2. The uncertainty is larger
190 in the cases with more electron populations, in particular when their parameters U_P are close.
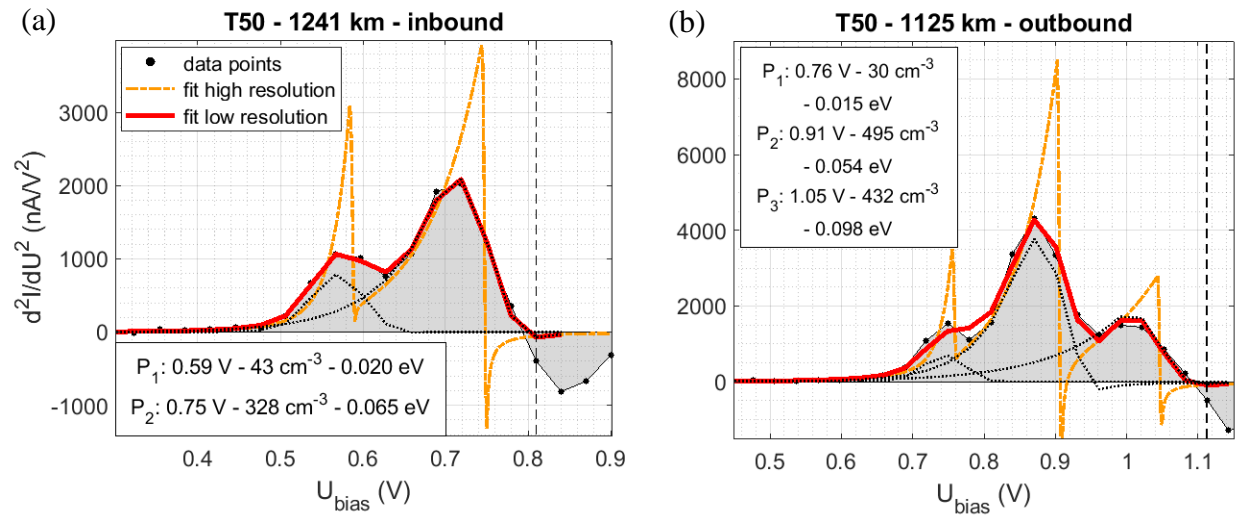
191

192

Figure 3. Second derivative of current for the sweeps shown in (a) Figures 1 and (b) Figure 2. The fitted
curves shown in Figures 1 and 2 are derived to obtain d²I/dU², at the resolution of the data points (red line)
and at higher resolution (orange dotted-dashed line). The fit results (U_p, n_e, T_e) for each population are
indicated on the graphs. The part of the curves after the dashed line corresponds to a part possibly distorted
by the effect of a logarithmic pre-amplifier, and should not be used without further consideration.

198

199

200   2.5 Link between the second derivative of the electron current and the Electron Energy
201   Distribution Function (EEDF)

202   This section explains the link between the second derivative of the current (d^2I/dU^2) and the
203   Electron Energy Distribution Function (EEDF). It aims to justify the attribution of electrons
204   populations to peaks in the second derivative. The presented method finally gives the Maxwellian
205   EEDF of each of the electron populations detected on a same measurement.

206

207   *2.5.1 The Druyvesteyn method*

208   The Druyvesteyn method (Druyvesteyn, 1930; Lieberman & Lichtenberg, 2005) was used to
209   compute the EEDF from the electron current measured by the Langmuir probe. The method is
210   valid for any convex probe geometry and does not depend on the probe dimension compared to
211   Debye length, or on the ratio T_i/T_e. The EEDF is computed from the second derivative of the
212   current, and the electron density is equal to the integral of the EEDF (see details in Appendix D):

$$EEDF_{Dr}(\Delta U) = \frac{2\sqrt{2}}{A_{LP}\,e^2}\sqrt{\frac{m_e\cdot(-\Delta U)}{e}}\;\frac{d^2 i}{d\Delta U^2}\qquad [J^{-1}.m^{-3}]$$

(6)

$$\text{with } n_e = \int_0^{+\infty} EEDF_{Dr}\big(E(\Delta U)\big).dE \quad and \quad E(\Delta U) = -e.\Delta U$$

213   If the Druyvesteyn method is applied to the expression of the current given in Equation (2), it gives
214   back the expression of an EEDF for a Maxwellian speed distribution:

$$EEDF_{Maxw}(E) = \frac{2}{\sqrt{\pi}}\cdot(k_B.T_e)^{-\frac{3}{2}}.n_e.\sqrt{E}.\exp\left(-\frac{E}{k_B.T_e}\right)$$

(7)

215

216   *2.5.2 EEDF: example with one population*

217   This section presents a simple case with one electron population (introduced in Figure S3 and
218   S5(a)). Figure 4 compares the EEDF obtained by applying the Druyvesteyn method to the data
219   points (Equation (6)), to the 'Maxwellian' EEDF computed with the fitted electron density and
220   temperature (Equation (7)). They do not perfectly match (the maximum of the peak is shifted)
221   because of the low resolution of the data points. Indeed, the Druyvesteyn method uses the second
222   derivative of the current, which is highly distorted because of the low number of data points (e.g.
223   the sharp initial increase is lowered by this effect).

224   To show this effect, the Druyvesteyn method is applied to the fit of the current. The EEDF obtained
225   using a fitting curve at high resolution (> 200 points per peak) superimposes very well with the
226   'Maxwellian' EEDF. On the other side, the EEDF obtained using a fitting curve with the resolution
227   of the Langmuir probe data points (4-10 points per peak) matches well with the EEDF obtained
228   from the data points. The EEDF obtained using the Druyvesteyn method on the Langmuir probe
229   data points is therefore fairly well represented by a 'Maxwellian' EEDF if one takes the problem
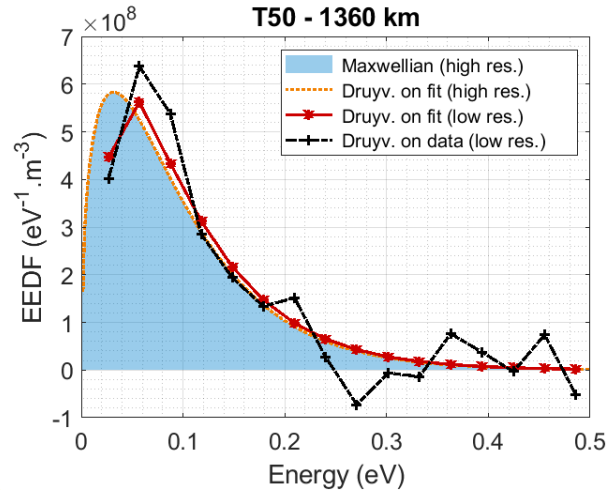230   of low resolution into account.

231

232

Figure 4. Example of EEDF obtained from Langmuir probe data with only one population using the Druyvesteyn method (dotted-dashed black line). Comparison to the EEDF obtained with the Druyvesteyn method applied to the fit at low resolution (red line), at high resolution (orange dotted line), and to the 'Maxwellian' EEDF from fitted n_e and T_e (blue area).

237

2.5.3 EEDF: example with several populations

In the case of data showing several populations, applying the Druyvesteyn method is less straightforward: the method requires one 'plasma potential' U_P, whereas the fit gives as much U_P as populations detected. Figure 5 shows the case of two populations. The Druyvesteyn method is applied to the data points using the U_P potential from (a) the first population and (b) the second population. In Figure 5b, the two population peaks appear in reverse order compared to the plot of d^2I/dU^2 in Figure 3a, because the x-axis is reversed ($E = -e \cdot \Delta U \propto -U_{bias} + U_P$).
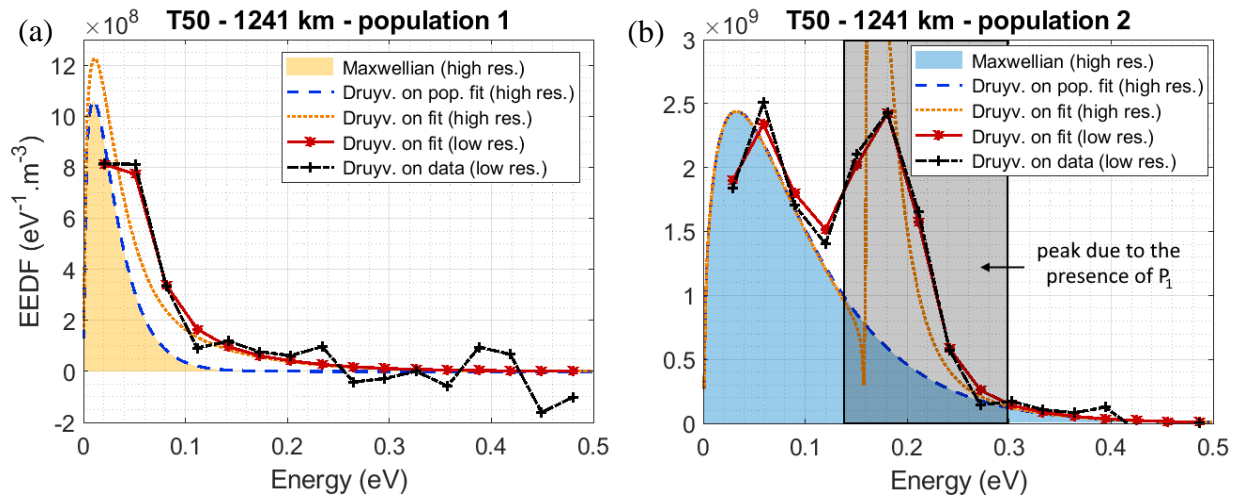
245

246

Figure 5. Example of EEDF obtained from Langmuir probe data with two populations using the Druyvesteyn method: (a) for population 1; (b) for population 2. Comparison of the EEDF using the Druyvesteyn method on data points (dotted-dashed black line) to the EEDF obtained with the Druyvesteyn method applied to the fit at low resolution (red line), at high resolution (orange dotted line), to the fit of

9

251   only one population at high resolution (dashed blue line) and to the 'Maxwellian' EEDF from fitted n_e and
252   T_e (area).

253

254   Figure 5 shows that in the case of several electron populations, the EEDF computed for one
255   population with the Druyvesteyn method is disturbed by the other populations with close values
256   of U_P. To observe this effect, the Druyvesteyn method is applied to the fit of the data points with
257   the two populations (orange line), and to the fitted current corresponding only to one population
258   (dashed blue line). Therefore, if one takes into account both the presence of nearby populations
259   (supplementary peak at higher energy) and the effects of low resolution (shift of the main peak),
260   the EEDF from data points can reasonably be modelled by a 'Maxwellian' EEDF (shaded area).
261   An example with 3 populations is given in Supporting Information Figure S6.

262

263   *2.5.4 Diversity of EEDF combinations for the different populations*

264   The 'Maxwellian' EEDF of the electron populations are compared in Figure 6. As mentioned in
265   Section 2.5.1, the area under each EEDF corresponds to the electron density of each population
266   and the position of the maximum of the EEDF is related to the electron temperature.

267   Figure 6 shows the variability of the electron distribution (i.e. the changes in electron populations)
268   for different flybys. It illustrates three very different cases obtained at ~1000 km altitude, which
269   are representative of the three flyby groups (G1, G2 and G3) presented in details below, in Section
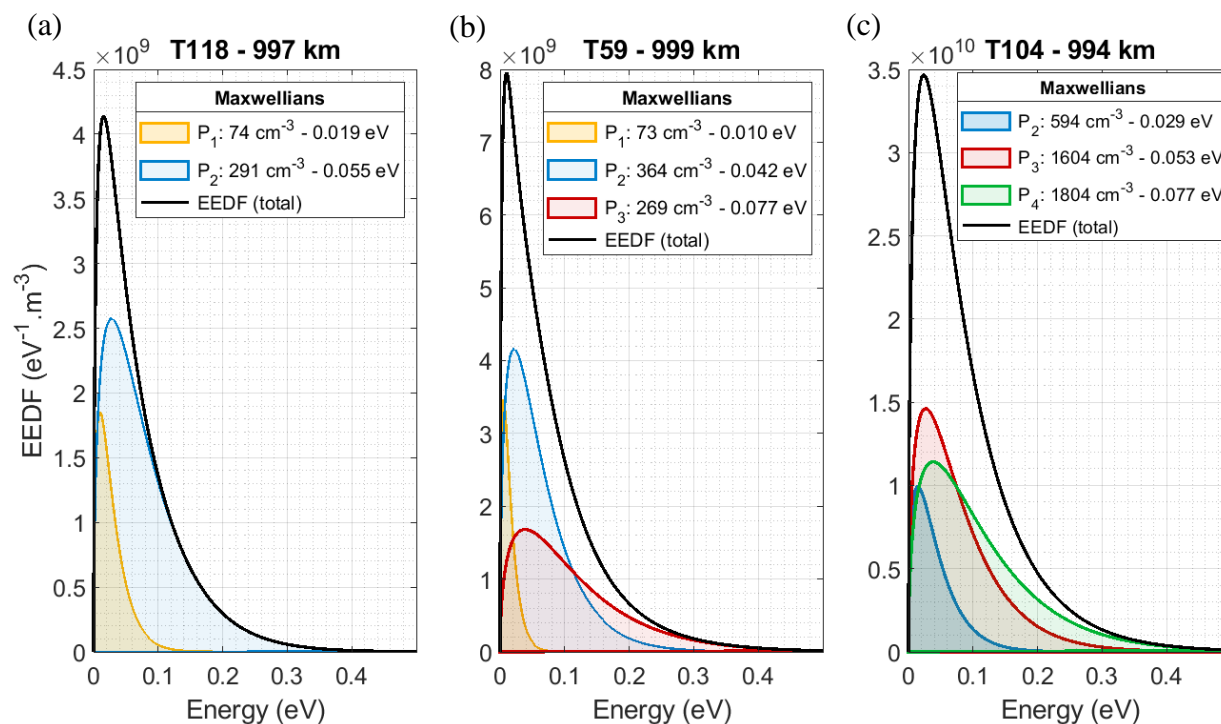270   3.1.

271

272   **Figure 6.** EEDF obtained from Maxwellian populations, at ~1000 km altitude for the flybys: (a) T118
273   (group G1); (b) T59 (G2); (c) T104 (G3).

274 The first case (from the group G1) shows two populations (named P_1 and P_2). The area (and so the
275 electron density) of P_2 dominates P_1. The second case (G2) has one additional population (P_3). The
276 area of P_2 and P_3 are equivalent and higher than the area of P_1. We observe that P_3 distribution is
277 in average at higher energy than the distribution of P_2: its electron temperature is higher. Finally,
278 the group G3 shows still another population (P_4) and P_1 becomes negligible compared to the others.
279 P_3 dominates P_2 in density. P_4 characteristics vary with altitude: it can be denser than the others,
280 and it is usually hotter.

281

282

283 **3 Results and discussions**

284   3.1 Variation of the electron populations with altitude and Solar Zenith Angle (SZA)

285   *3.1.1 Variation with altitude*

286 Voltage sweeps evolve during a flyby. The number of observed peaks in the second derivative of
287 the current (d^2I/dU^2) varies with altitude. Therefore, the number of electron populations (and
288 consequently the electron distribution) changes with altitude for a given flyby. We focus on the
289 part of the ionosphere below 1200 km. The Langmuir probe took measurements at these altitudes
290 at the occasion of 57 flybys.

291 The curves of d^2I/dU^2 as a function of the altitude obtained from the 57 flybys allow to easily
292 classify Titan flybys in three groups. Each group has a different number of electron populations,
293 with different characteristics. They are described in Table 1 and examples of profiles for the three
294 cases are shown in Figure 7. All the profiles have similar d^2I/dU^2 curves around 1250-1200 km,
295 showing usually three peaks. However, this curve evolves differently with altitude in the three
296 cases. At lower altitude, in all cases, there is a main hump formed either by one large peak, two or
297 three peaks (further named P_1, P_2, P_3 for clarity). In addition, for the profiles of the group G3, a
298 small hump detached from the main one (P_4), at higher voltage, is observed below ~1200 – 1150
299 km altitude.

300

301 **Table 1.** Definition of the 3 flyby groups and their corresponding flybys. The flybys studied in details in
302 Figure 7 and Scetion 3.2 are indicated in bold.

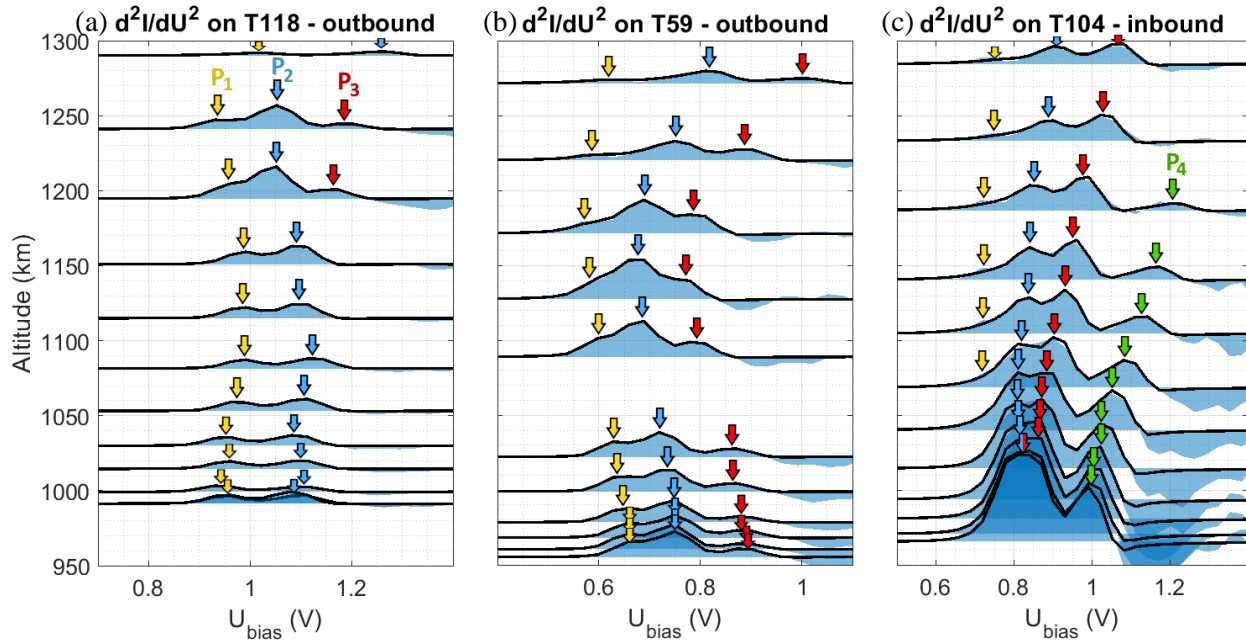| Name of the flyby group	Characteristics of d^2I/dU^2 at lower altitude	Flybys (T#)
G1	2 separated peaks	21, 25-28, 55, **118**-119
G2	3 peaks	5, 16, 46, 50, 56-**59**, 65, 117, 121
G3	1 large peak (or 2 close) + 1 further, at higher U_{bias}	17, 20, 23, 39-43, 47-48, 51, 83-88, 91-92, 95, 100, **104**, 106-108, 113, 126
G1/G2	with different characteristics on inbound and outbound	29-30, 32, 120
G2/G3		18-19, 36, 49, 61, 70-71

303

304

11

305

Figure 7. Examples of d²I/dU² profiles with altitude: (a) T118 (from G1), (b) T59 (G2) and (c) T104 (G3).
The second derivative of the electron current from Langmuir probe data (blue area) is superimposed to
d²I/dU² from the fit (black line). The scaling of d²I/dU² is the same for all the plots. Arrows indiquate the
peaks corresponding to the 4 populations.

310

311   *3.1.2 Variation with Solar Zenith Angle (SZA)*

312   The detection of populations P_3 and P_4 are strongly dependent on the Solar Zenith Angle (SZA).
313   Figure 8 shows the repartition of the electron populations with altitude and SZA in the case of 57
314   Cassini flybys. The population P_4 appears always below ~1200 km and at SZA < 80-90° (such
315   flybys belong to the group G3), and the cases without a P_3 population at lower altitude (group G1),
316   are observed only on the nightside, at high SZA (>~120°).

317   The distribution of the 57 flybys in three groups is then closely correlated to their SZA. The group
318   G1 corresponds to flybys on the far nightside (SZA >~120°), G2 to flybys on nightside close to
319   the terminator, and G3 to dayside (SZA < 80-90°).

320   In conclusion, the variation with altitude and SZA of the detected peaks of d²I/dU² can be
321   schematized as in Figure 9. Each peak is attributed to an electron population among P_1, P_2, P_3 and
322   P_4. At ~1200-1300 km, d²I/dU² graphs are very similar at all SZA, with three populations (P_1, P_2,
323   P_3). Below 1200 km, d²I/dU² varies differently depending on SZA: (G1) on the far nightside (SZA
324   >~120°), P_3 disappears; (G2) close to the terminator, the three populations are kept at lower
325   altitudes, with an increase of the area of the P_2 peak; (G3) and on dayside, P_2 and P_3 grow, P_1
326   becomes negligible and P_4 appears. In some occasions, P_2 and P_3 peaks merge.
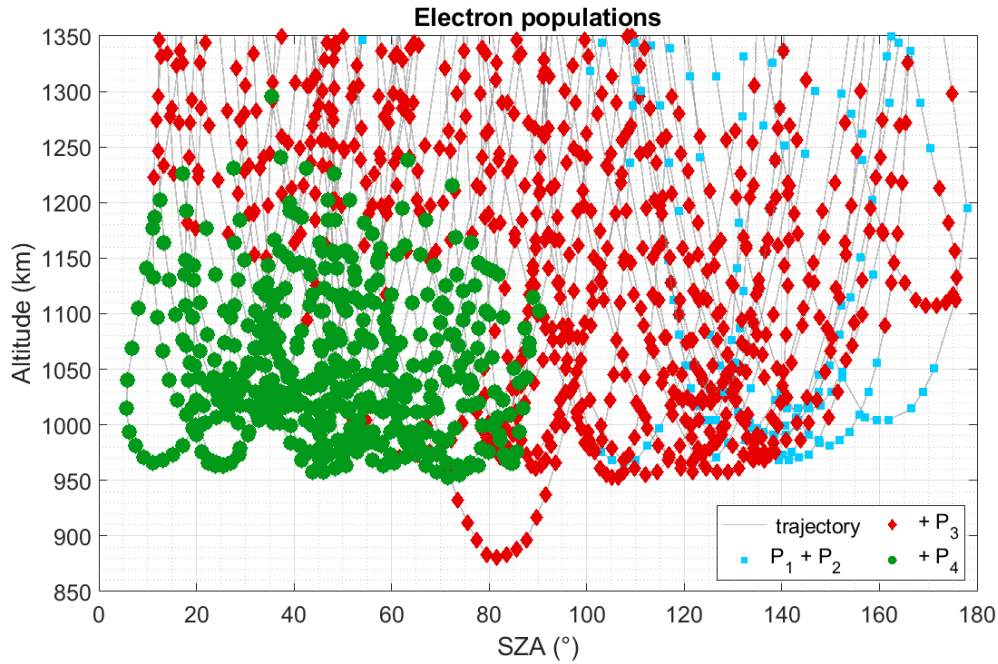
327

328

329   **Figure 8.** Detection of electron populations as a function of altitude and SZA, from 57 flybys. Blue squares
330   represent sweeps with only populations P_1 and P_2, red diamonds show the presence of P_3, and green dots
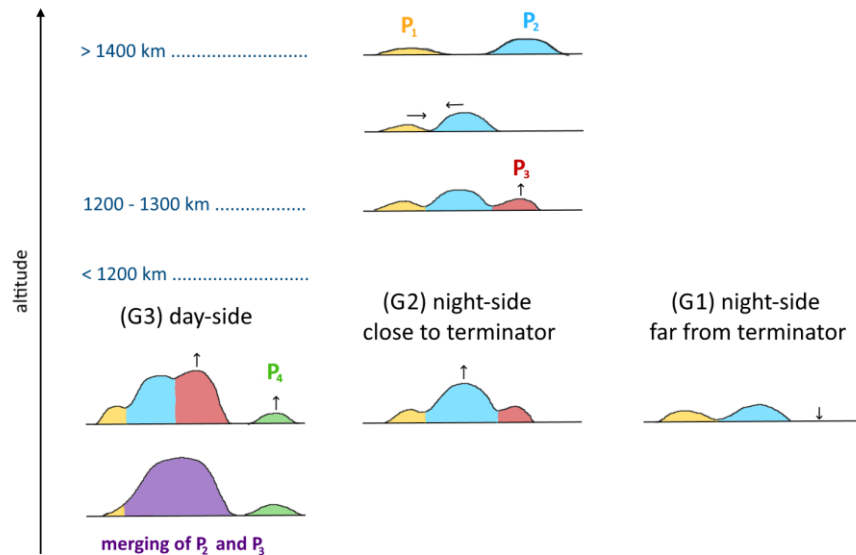331   are for P_4.

332

333

334   **Figure 9.** Summary scheme of the evolution of d^2I/dU^2 peaks with altitude in the 3 cases: nightside far from
335   terminator (G1), nightside close to terminator (G2) and dayside (G3). Small arrows indicate the evolution
336   trends with decreasing altitude.

337

338   3.2 Electron densities and temperatures

339   The results on electron density and temperature are discussed separately for each of the 3 groups
340   (G1, G2 and G3), in the following sub-sections (respectively 3.2.1, 3.2.2 and 3.2.3).

341   *3.2.1 Nightside far from the terminator (group G1)*

342   *3.2.1.1 Typical altitude profiles*

343   Figure 10 shows inbound (solid lines) and outbound (dashed lines) profiles of the electron density
344   and temperature typical of the far nightside (G1). The confidence interval at 95% is indicated with
345   shaded areas (see computation in Appendix C). The dominant population observed is P_2 (blue),
346   with a rather constant temperature around 40-60 meV (460-700 K) below 1150-1250 km altitude.
347   The density of this population peaks at an altitude varying between 1150 and 1250 km altitude.
348   The population with the lowest U_p (P_1, orange) is very constant with altitude. Its density is low,
349   less than 100 cm^{-3}. Its temperature is around 10-20 meV (120-230 K), at the detection limit of the
350   probe. In addition, a third population appears (P_3, red) at the ionospheric peak, when the total
351   electron density exceeds 500 cm^{-3}. It has a temperature higher than the other populations, around
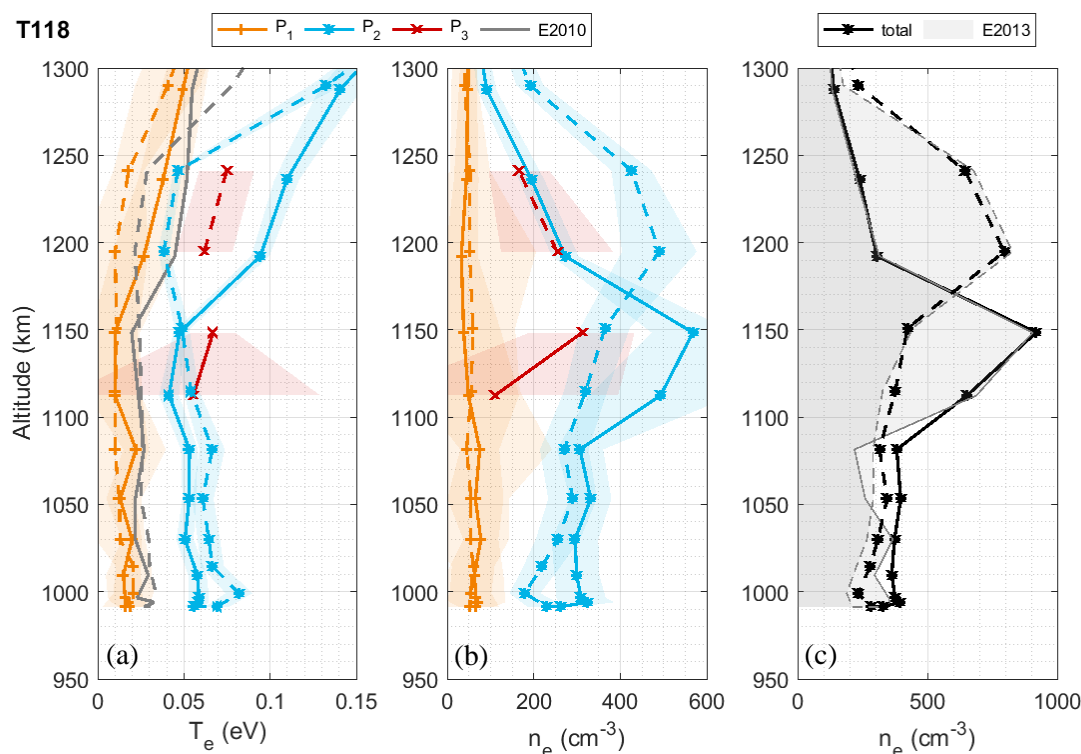352   60-90 meV (700-1040 K).

353

354   **Figure 10.** Electron temperature (a) and density (b,c) profiles in the case of T118, an example of a G1 group
355   flyby (far nightside); inbound (line) and outbound (dashed line); results for the different populations P_1, P_2
356   and P_3 (colors). The fit confidence intervals at 95% are indicated in colored shaded area. The total density
357   (sum of the densities of all the populations) is indicated in black. Comparison to Edberg et al. (2013, 2010),
358   respectively noted E2013 and E2010 (grey).

359

14

360 The total electron density obtained is consistent with previous measurements acquired with
361 different methods (Ågren et al., 2009; Edberg et al., 2013; Garnier et al., 2009). The comparison
362 of our fit to the density measurements by Edberg et al. (2013) serves as a validation tool. As for
363 electron temperature, results are compared to a previous analysis (Edberg et al., 2010). This
364 previous analysis usually gives an electron temperature between the ones found for P_1 and P_2, and
365 therefore sometimes colder than the dominant population (P_2) temperature. For instance, in the
366 case of T118 shown in Figure 10, they obtained a temperature not representative of the main
367 population of electrons (P_2). It shows that using several electron populations in the fitting of the
368 sweeps significantly improves the analysis, since it attributes a temperature for each population,
369 and consequently, the temperature of the dominant electron population can be found without
370 ambiguity.

371

372 *3.2.1.2 Necessity to fit multiple populations*

373 Even if the population P_1 is not abundant, it is necessary to fit it separately from the main
374 population P_2 to avoid a hot bias on the determination of the temperature of P_2. For comparison,
375 we studied the case where the current curve is fitted using only one population, as shown in Figure
376 1a. The results are compared in Figure 11. Forcing only one electron population (P_2, dark blue)
377 overestimates the temperature of the dominant population (P_2, light blue) by ~0.01 eV (~120 K).
378 In addition, the total electron density increases of ~10% and is no longer consistent with the density
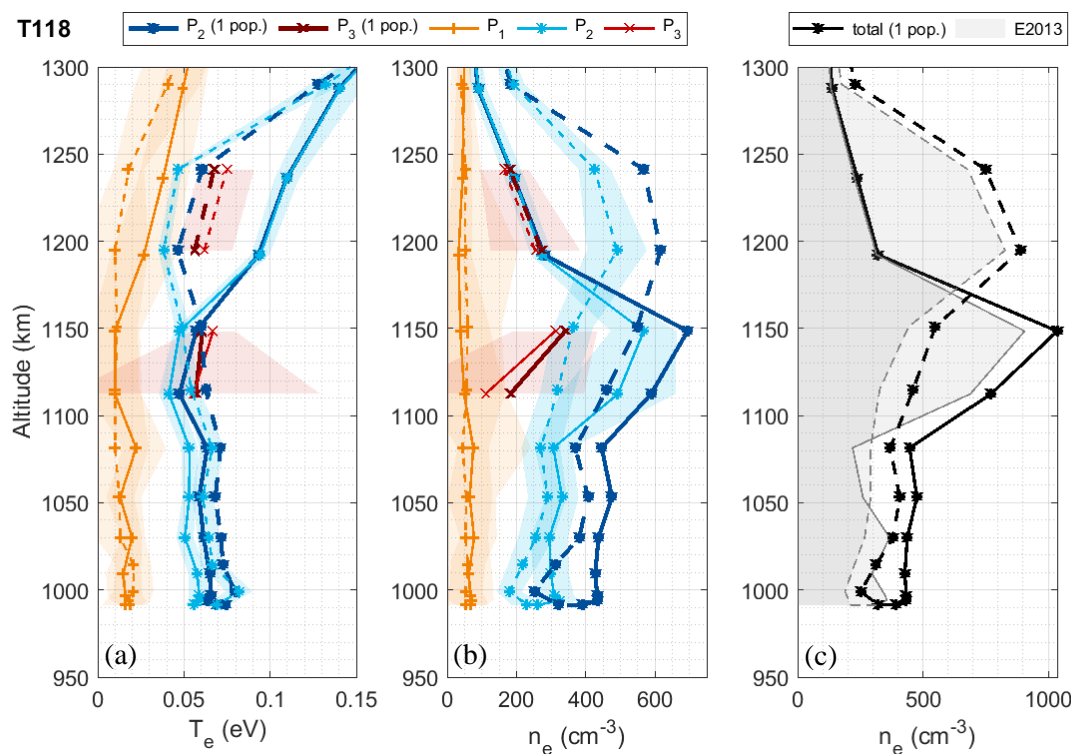379 measured by Edberg et al. (2013).

380

381 **Figure 11.** Same as Figure 10, superimposed to the T_e and n_e profiles obtained with only one population to
382 fit P_1 and P_2 when their potentials are close enough (i.e. below 1200 km for inbound, and below 1300 km
383 for outbound).

15

384

3.2.1.3 Discussion on the origin of P_1 and P_2

386 On the nightside far from the terminator, ionization is not governed by solar photons, but by
387 energetic particles coming from the magnetosphere (Ågren et al., 2007; Cravens et al., 2008). We
388 therefore assume that the dominant electron population (P_2) is the bulk of thermalized electrons
389 initially formed by energetic magnetospheric particles.

390 The other population present at all altitudes, P_1, is certainly due to electrons emitted by the nearby
391 probe boom, from collisions with energetic particles. Such electrons are created on the nearby
392 surfaces, they have low energy and are easily caught back. Therefore, P_1 corresponds to the
393 population with the lower potential U_p.

394 P_3 is discussed in the following sections, as it is observed in higher quantities in groups G2 and
395 G3.

396

3.2.2 Nightside close to the terminator (group G2)

3.2.2.1 Typical altitude profiles

399 Flybys on the nightside close to the terminator (~90° < SZA ~< 140°) show the presence of the
400 third population at all altitudes (see Figure 12).
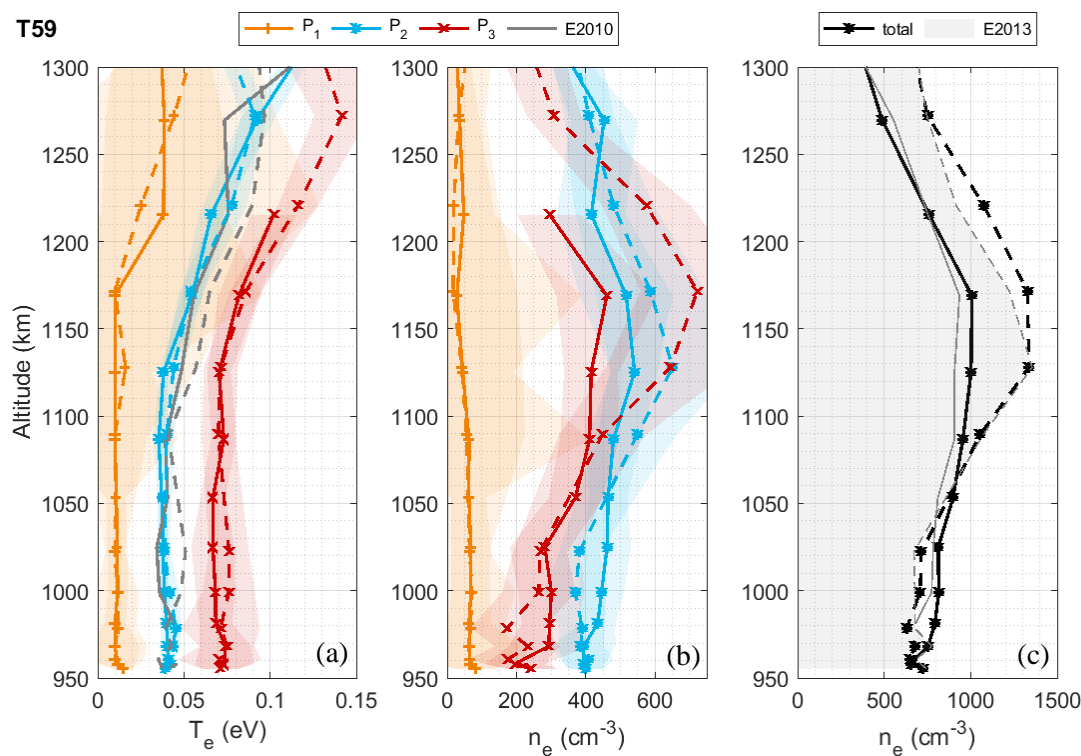

401

402 **Figure 12.** Same as Figure 10, in the case of T59, an example of a G2 group flyby (nightside close to the
403 terminator).

16

404

405 The total electron density is globally higher than for G1 flybys (far nightside), which is expected
406 because of the closer influence of photoionization on dayside (Ågren et al., 2009). The
407 temperatures observed for the three populations are similar to the ones of G1 flybys: P_1 below 20
408 meV (~230 K, orange), P_2 generally between 30 and 50 meV (350-580 K, blue) and P_3 at 60-80
409 meV (700-930 K, red).

410

411   *3.2.2.2 Necessity to fit multiple populations*

412 The addition of the third population (P_3) does not disturb the fitting of the two first populations.
413 Besides, it is necessary to include it to obtain a total electron density similar to Edberg et al. (2013).
414 This effect is showed in Figure 13. It compares the results obtained in Figure 12 with results of a
415 fit that does not include the population P_3, as plotted in Figure 2 (a). Then, the temperatures
416 obtained for P_1 and P_2 are almost unchanged, but the total electron density decreases of 25%.
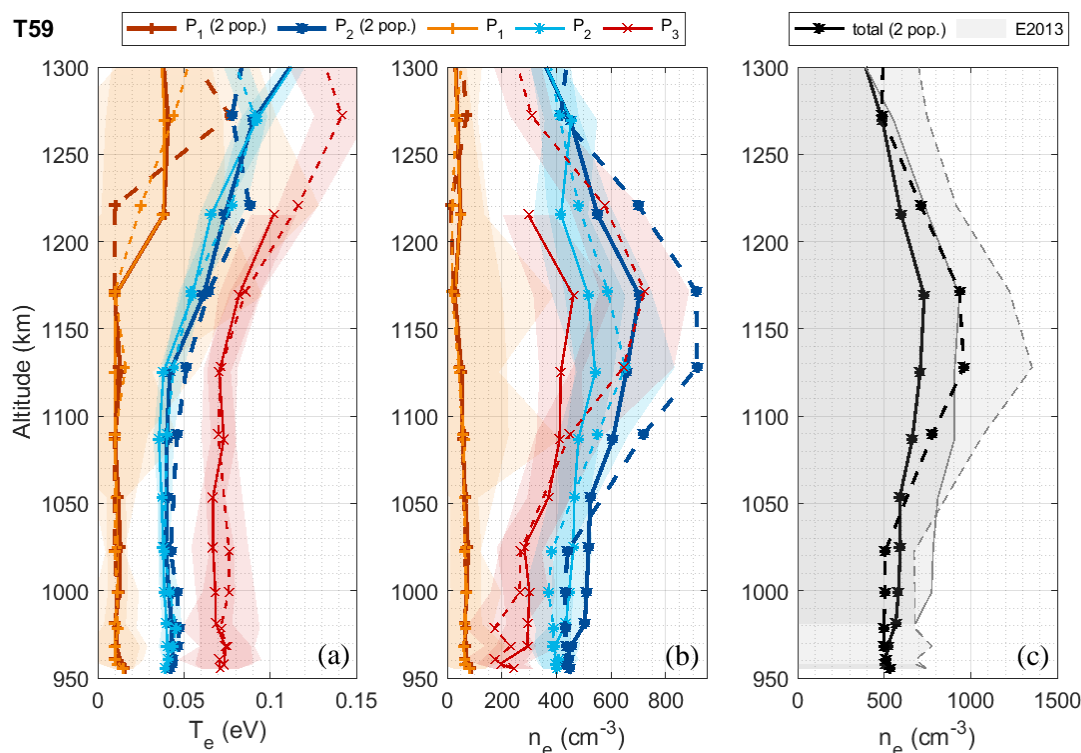
417

419 **Figure 13.** Same as Figure 12, superimposed to the T_e and n_e profiles obtained for P_1 and P_2 when P_3 is not
420 fitted.

421

422   *3.2.2.3 Discussion on the origin of P_3*

423 The fact that P_3 is observed on dayside (G3) but not on the far nightside (G1), suggests that it is
424 due to the efficient photo-ionization processes happening on the dayside, whose influence is

425 extended by transport as far as the nightside close to the terminator. However, one should also
426 consider a possible effect of the active ion chemistry happening in these regions on the
427 characteristics of the electron population P_3. In particular, the ionosphere environment on the
428 nightside close to the terminator is enabling the growth of large ions, which is otherwise disrupted
429 under direct extreme UV fluxes (Shebanits et al., 2017b, 2017a; Wellbrock et al., 2019).

430

431

432   *3.2.3 Dayside (group G3)*

433   *3.2.3.1 Typical altitude profiles*

434 On dayside, a new population (P_4) appears in the LP sweep data at a potential U_P higher than for
435 P_1, P_2 and P_3. Its temperature is generally higher than for the other populations, up to 0.1 eV (~1160
436 K, green). This population appears only at altitudes below ~1200-1150 km and its density increase
437 with decreasing altitude. In some cases (T17, T20, T85, T88, T104, T108), it even becomes the
438 dominant population below 1050-1000 km, as shown in Figure 14. Contrary to the constant
439 profiles on the nightside, the temperatures of all the populations decrease slightly with altitude, of
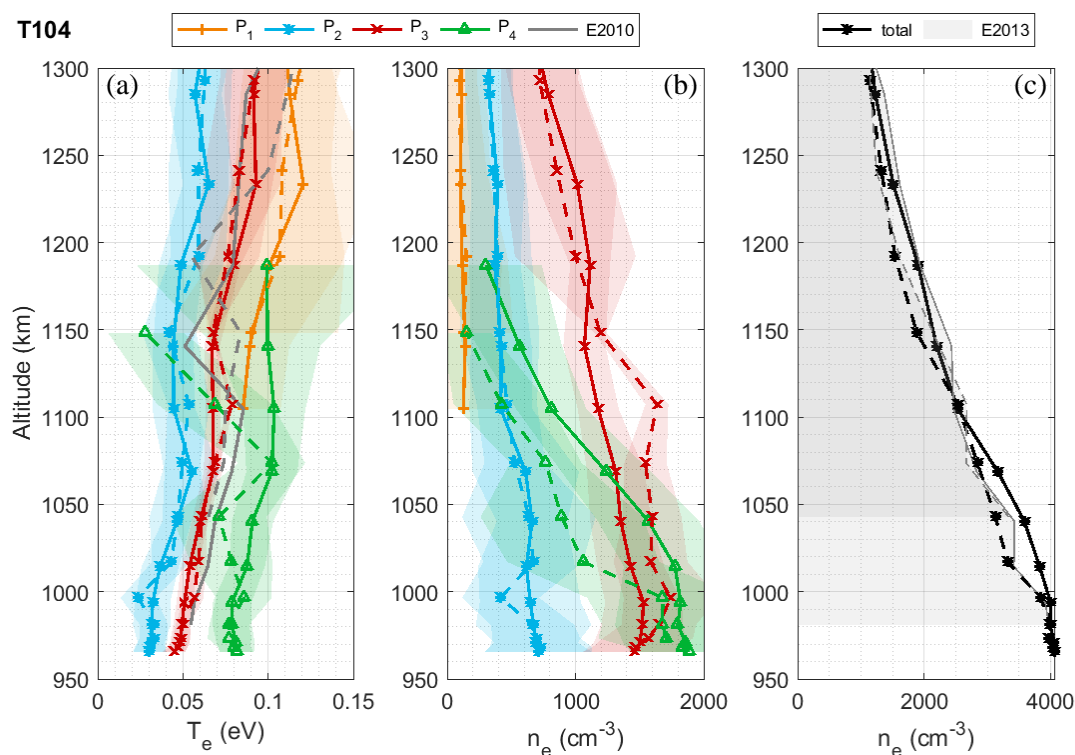440 ~0.03 eV (~350 K) in 200 km.

441

442
443 **Figure 14.** Same as Figure 10, in the case of a T104, an example of a G3 group flyby (dayside).

444

18

445   *3.2.3.2 Necessity to fit P_4 and fusion of P_2 and P_3*

446   The electron population P_4 is often non-negligible and should always be taken into account when
447   present. An example of the results obtained if P_4 is not fitted is given in Supporting Information
448   Figure S7. The results are similar to Section 3.2.2.2: the (U_p, n_e, T_e) results for the other populations
449   are not impacted, but the total electron density is underestimated by up to 30%.

450   In some cases, the fitting of P_2 and P_3 can be ambiguous, especially at lower altitudes. The use of
451   two distinct populations is required to obtain a very good fitting (examples of sweeps are given in
452   Supporting Information Figure S8) and is consistent across all altitudes (see Figure 7 for T104).
453   Nevertheless, the fusion of P_2 and P_3 at lower altitudes in G3 flybys happens smoothly: at one
454   point, fitting with two or three populations gives globally the same results: P_2 becomes negligible
455   compared to P_3. An example of the n_e and T_e profiles obtained when P_2 and P_3 are fitted by only
456   one population at lower altitude is given in Supporting Information Figure S9. The total electron
457   density stays globally the same, the temperature of the main population is not impacted and the
458   population P_4 generally stays in the range of its large error bars.

459

460   *3.2.3.3 Discussion on the origin of P_1 and P_4*

461   Similarly to the nightside, P_1 electrons on the dayside are certainly emitted by the probe boom.
462   However, on dayside, the photoemission is also possible. In this case, the emitted electrons
463   observed are hotter than on nightside.

464   The population P_4 is only detected on dayside. We argue here that it is not an instrumental effect
465   but rather due to dusty plasma:

466   - Energetic photons and particles can detach electrons from the surface of the spacecraft.
467   Nevertheless, in the ionosphere the electrons are cold enough to prevent these spacecraft
468   electrons to reach the Langmuir probe (Wang et al., 2015). Indeed, the Debye length in the
469   ionosphere is always below 10.5 cm, far lower than the distance between the spacecraft and
470   the Langmuir Probe (which is on a 1.5 m boom).

471   - The spacecraft motion cannot explain the presence of several electron populations. With
472   energies from 0.02 to 0.08 eV in the ionosphere, the electrons of the various populations have
473   a thermal velocity of 85 to 170 km/s, much larger than the spacecraft velocity (~6 km/s).
474   Therefore, there should be no difference in the electron collection from all around the probe.

475   - The perturbation of the collected current by organic deposit on the surface of the probe is not
476   likely. In theory, the complex organic chemistry happening in the ionosphere could possibly
477   lead to the formation of a deposit on the surface of the probe during the 10-15 minutes long
478   ionosphere pass. Such a film coating, depending on the surface coverage and dielectric
479   properties, would induce the detection of several electron components in the sweeps. However,
480   no indication of this has been observed when comparing the sweeps 'down' and 'up' (see
481   Section 2.1, Appendix A and Supporting Information Figure S1). Additionally, the probe is
482   cleaned between two flybys (see Section 2.1), and observations during the inbound and the
483   outbound are very similar (in the case of flybys with inbound and outbound at similar SZA).

484   - P_4 is possibly due to a dusty plasma effect. Indeed, it is not predicted by current ionospheric
485   models that do not include the effect of the charged dust grains or aerosols on the electron

486 populations. The fourth electron population is only detected in the regions where dusty plasma
487 has been previously measured (Shebanits et al., 2016), this suggests the charged dust grains to
488 be the cause, either as a source or a disruption of the ambient electrons. This possibility is
489 investigated in paper II.

490

491

492 **4 Conclusions**

493 The re-analysis of the Langmuir probe data in Titan's ionosphere brought new insights on the
494 behavior of the electrons in this environment.

495 The detailed analysis of the data revealed the presence of several electron populations, at different
496 potentials, and with different electron densities and temperatures. We have shown that the second
497 derivative of the electron current collected by the Langmuir probe during a voltage sweep is a
498 useful tool to detected the presence of several electron populations, especially as it is linked to the
499 electron energy distribution function (EEDF) (Druyvesteyn, 1930). With the evolution of the
500 second derivative of the current with altitude we observed the evolution of the electron populations
501 with altitude in three different conditions: far nightside (T118), nightside close to the terminator
502 (T59) and dayside (T104).

503 Two populations (with the lower potentials) are present in nearly all conditions. The third
504 population is not observed on the far nightside, and the fourth is detected on dayside below 1200-
505 1150 km. We have investigated the fitting of the electron current curve with 2 to 4 populations
506 with a systematic approach on all flybys that validated the presence of 2, 3 or 4 populations only
507 depending on the altitude and the solar illumination. A rigorous testing on the number of fitted
508 populations shows that the fitting of all the detected populations (i.e. the whole electron
509 distribution) is necessary to obtain a correct fit and retrieve the total electron density previously
510 deduced from different methods (Ågren et al., 2009; Edberg et al., 2013; Garnier et al., 2009).

511 We suggested possible origins for the four populations:

512 - P_1 electrons, with the lowest potential and a low density, are emitted by the probe boom;
513 - a likely cause for the P_2 electrons, found even on the far nightside, is the thermalization of
514 magnetospheric electrons;
515 - P_3 electrons, not present on the far nightside, are likely to be related to photo-ionization;
516 - and P_4 electrons, observed at lower altitudes on dayside, are plausibly linked to dusty
517 plasma effects.

518 These four populations are studied in more details in paper II that performs a complete
519 investigation on all the Cassini Langmuir probe dataset in the ionosphere of Titan.

520

521

522

533
534

535 **Appendix A.**

536 We investigated the reproducibility of the measurements with the two voltage sweeps (named
537 'down' and 'up'), and the double measurements at each voltage step (resp. 'down1'-'down2' and
538 'up1'-'up2'). Figure A1 shows the comparison.
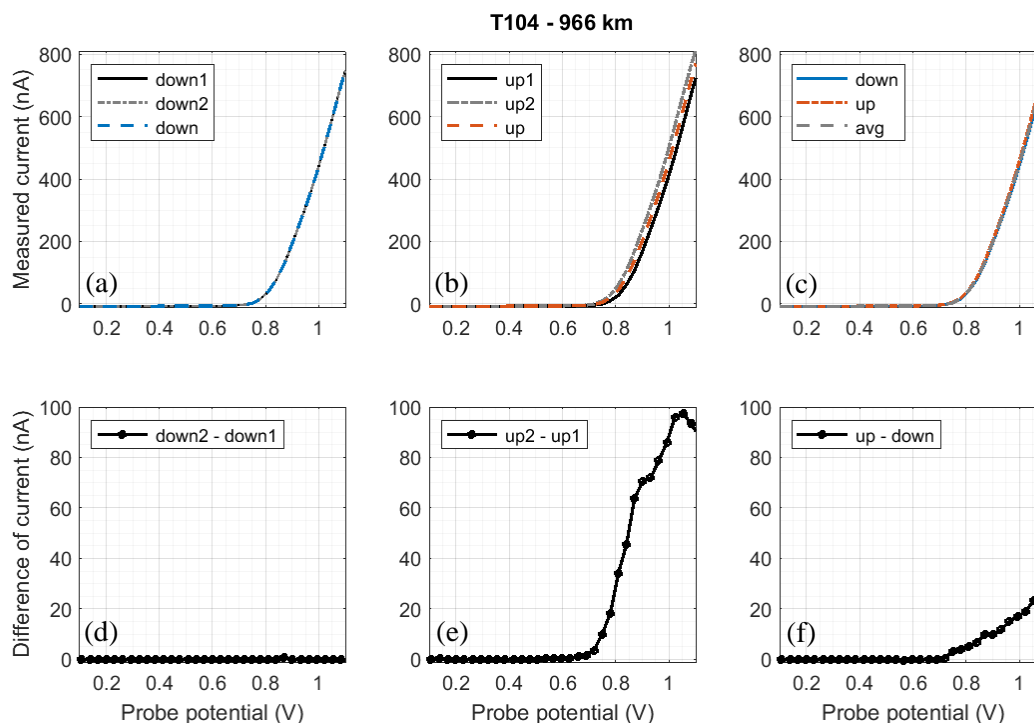
539
540 **Figure A1.** Raw data of the acquisition of a LP sweep. Left: data from the decreasing phase: (a) first point
541 acquired ('down1'), second point acquired ('down2'), the average of both ('down') and (b) their difference
542 ('down2 – down1'). Middle: the same for the increasing phase, respectively (b) and (e). Right: (c) the
543 average for the decreasing and increasing phases, the average of both ('avg') and (f) their difference ('up –
544 down'). From a measurement at ~966 km, during the Titan flyby T104.

545

546   The two data points taken at a same voltage step during the decreasing voltage phase ('down1'
547   and 'down2') are always very close to each other: the current stabilizes quickly at after each
548   voltage step. However, during the increasing voltage phase ('up1' and 'up2'), the current continues
549   to increase between the two measurements: the current takes longer to stabilize, especially in the
550   strongly varying exponential parts of the sweep.

551   Figure A2 shows the variations 'down2 – down1', 'up2 – up1' and 'up – down' with altitude for
552   26 flybys on dayside and 8 flybys on nightside far from the terminator. In each case, we selected
553   the largest difference of current and the maximum of the averaged current in the voltage range
554   [Up1 – 0.7, Up1 + 0.3], Up1 being the plasma potential of the first population (it is located at the
555   beginning of the increase of the current and is more precisely defined below). Figure A2 shows
556   their ratio (difference / average) as a function of altitude. In all cases, the difference 'down2 –
557   down1' (blue triangles) is very small, as opposed to 'up2 – up1' (orange squares) that ranges from
558   9 to 23%. The difference 'up – down' (black stars) is often negative, and inferior to 10% in absolute
559   values.

560   The difference between 'up1' and 'up2' shows that the collected current is not stabilized, and
561   increases between the acquisition of the two points on a same voltage step. On nightside flybys
562   (Figure A2b), the difference 'up2 – up1' varies smoothly with altitude, while on dayside flybys
563   (Figure A2a) a sudden change in the difference is always observed between 1100 and 1200 km.

564

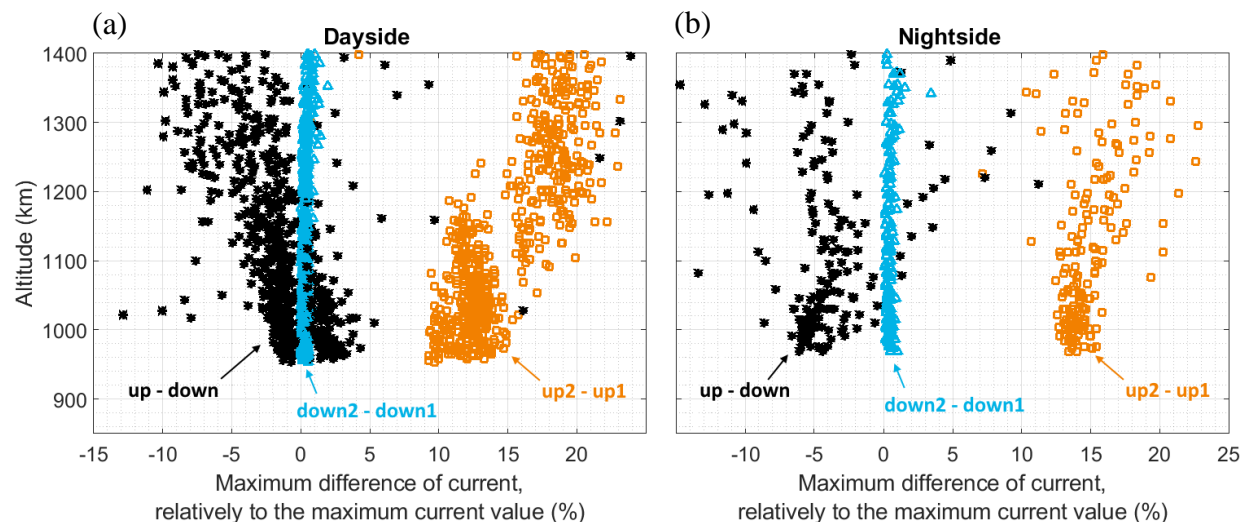565   **Figure A2.** Maximum differences of the current ('down2 – down1', 'up2 – up1' and 'up – down') in the
566   voltage range [Up1 – 0.7, Up1 + 0.3] as a function of altitude. The maximum differences are divided by the
567   maximum of the averaged current to facilitate the comparison at different altitudes. (a) Flybys on dayside.
568   (b) Flybys on nightside, far from the terminator.

569

570

571

572

573

574   **Appendix B. Algorith to fit the voltage sweeps with several populations**

575   To constrain the fitting of voltage sweeps in the case of several electron populations, the following
576   procedure is used:

577   1/ detection of the increase of the current (generally above 0.8 nA) and of the saturated part
578   (U_{lim});

579   2/ search for peaks in the second derivative of the current (d^2I/dU^2) in the voltage interval
580   defined in 1/;

581   3/ selection of the part of the voltage sweep (I_1) with a voltage inferior to the potential
582   corresponding to the minimum of d^2I/dU^2 between the two first peaks (or $< U_{lim}$ if there is only
583   1 population);

584   4/ fit of the current curve for the first population with Equations (2) and (5) in the reduced
585   voltage interval I_1;

586   If there is more than 1 population:

587   5/ selection of the part of the curve (I_2) with a voltage inferior to the potential corresponding
588   to the minimum of d^2I/dU^2 between peak 2 and peak 3 (or $< U_{lim}$ if there are only 2
589   populations);

590   6/ fit of populations 1 and 2 with two set of Equations (2) and (5) in the reduced voltage
591   interval I_2, the initial parameters for the fit of the first population being given by 4/;

592   If there are more than 2 populations:

593   7/ selection of the part of the curve (I_3) with a voltage inferior to the potential corresponding
594   to the minimum of d^2I/dU^2 between peak 3 and peak 4 (or $< U_{lim}$ if there are only 3
595   populations);

596   8/ fit of populations 2 and 3 with two set of Equations (2) and (5) in the reduced voltage
597   interval I_3, the initial parameters for the fit of population 2 being given by 6/. The contribution
598   of population 1 is beforehand removed, based on the fit results in 6/;

599   If there are more than 3 populations:

600   9/ selection of the part of the curve (I_4) with a voltage inferior to U_{lim};

601   10/ fit of populations 3 and 4 with two set of Equations (2) and (5) in the reduced voltage
602   interval I_4, the initial parameters for the fit of population 3 being given by 8/. The contributions
603   of populations 1 and 2 are beforehand removed, based on the fit results in respectively 6/ and
604   8/;

605

606

607

608   **Appendix C. Confidence intervals for fit results**

609   The parameters fitted are not directly (U_P, n_e, T_e), but $(U_P, I_0, \beta = 1/T_e)$, with T_e the electron
610   temperature in electron volt. The confidence intervals for the last three parameters are obtained at

611　95%. The standard deviation is then easily deduced for U_P and T_e. Concerning n_e, the standard
612　deviation (σ_{n_e}) is obtained by the following equation, derived from Equation (3) applied to
613　electrons:

$$\sigma_{n_e} = \left(\frac{\sqrt{2\pi m_e}}{A_{LP} e^{3/2}} \right) \times \left(\sigma_{I_0} . \sqrt{\beta} + I_0 . \frac{\sigma_\beta}{2\sqrt{\beta}} \right) \tag{C-1}$$

614　with I_0 and β obtained by the fit, and σ_{I_0} and σ_β their standard deviations.

615

616

617

618　**Appendix D. Equation linking the EEDF to the second derivative of the current (Druyvesteyn**
619　**method)**

620　The equation for the electron velocity distribution as function of the second derivative of the
621　electron current is given by the equation (3) in Druyvesteyn (1930):

$$\mathcal{V}(\Delta U) = \frac{4\,m_e}{A_{LP}\,e^2} \cdot \Delta U \cdot \frac{d^2 I_e}{d\Delta U^2} \qquad [(m.s^{-1})^{-1}.m^{-3}] \tag{D-1}$$

622　Electrons with a speed between v and $v + dv$ have energies between E and $E + dE$, therefore:

$$\mathcal{V}(v). dv = EEDF(E). dE \tag{D-2}$$

623　The derivative of the speed with respect to energy is given by:

$$E = \frac{1}{2} m_e v^2 \quad => \quad \frac{dv}{dE} = (2m_e E)^{-\frac{1}{2}} \tag{D-3}$$

624　Therefore, we obtain the EEDF by dividing the electron speed distribution by $\sqrt{2m_e E}$, with
625　$E(\Delta U) = -e . \Delta U$:

$$EEDF_{Dr}(\Delta U) = \frac{2\sqrt{2}}{A\,e^2} \sqrt{\frac{m.(-\Delta U)}{e}} \frac{d^2 i}{d\Delta U^2} \qquad [J^{-1}.m^{-3}]$$

$$\text{with } n_e = \int_0^{+\infty} EEDF_{Dr}\big(E(\Delta U)\big) . dE \tag{D-4}$$

626

627

628

629

630 **References**

631

632 Ågren, K., Wahlund, J. E., Modolo, R., Lummerzheim, D., Galand, M., Müller-Wodarg, I., et al.
633   (2007). On magnetospheric electron impact ionisation and dynamics in Titan's ram-side and
634   polar ionosphere - a Cassini case study. *Annales Geophysicae*, *25*(11), 2359–2369.
635   https://doi.org/10.5194/angeo-25-2359-2007

636 Ågren, K., Wahlund, J.-E., Garnier, P., Modolo, R., Cui, J., Galand, M., & Müller-Wodarg, I.
637   (2009). On the ionospheric structure of Titan. *Planetary and Space Science*, *57*(14–15),
638   1821–1827. https://doi.org/10.1016/J.PSS.2009.04.012

639 Bettinger, R. T., & Walker, E. H. (1965). Relationship for Plasma Sheaths about Langmuir Probes.
640   *The Physics of Fluids*, *748*(8), 748–751. https://doi.org/10.1063/1.1761293

641 Chatain, A., Wahlund, J. -E., Shebanits, O., Hadid, L. Z., Eriksson, A. I., Morooka, M. W., et al.
642   (n.d.). Re-analysis of the Cassini RPWS/LP data in Titan's ionosphere. Part II: statistics on
643   57 flybys. *Journal of Geophysical Research: Space Physics*, *submitted*.

644 Coates, A. J., Crary, F. J., Lewis, G. R., Young, D. T., Waite, J. J. H., & Sittler, J. E. C. (2007).
645   Discovery of heavy negative ions in Titan's ionosphere. *Geophysical Research Letters*, *34*,
646   L22103. https://doi.org/10.1029/2007GL030978

647 Cravens, T. E., Robertson, I. P., Ledvina, S. A., Mitchell, D., Krimigis, S. M., & Waite, J. H.
648   (2008). Energetic ion precipitation at Titan. *Geophysical Research Letters*, *35*(3), L03103.
649   https://doi.org/10.1029/2007GL032451

650 Cravens, T. E., Robertson, I. P., Waite, J. H., Yelle, R. V., Vuitton, V., Coates, A. J., et al. (2009).
651   Model-data comparisons for Titan's nightside ionosphere. *Icarus*, *199*(1), 174–188.
652   https://doi.org/10.1016/j.icarus.2008.09.005

653 Cui, J., Galand, M., Yelle, R. V., Vuitton, V., Wahlund, J. E., Lawas, P. P., et al. (2009). Diurnal
654   variations of Titan's ionosphere. *Journal of Geophysical Research: Space Physics*, *114*,
655   A06310. https://doi.org/10.1029/2009JA014228

656 Druyvesteyn, M. J. (1930). Der niedervoltbogen. *Zeitschrift Für Physik*, *64*(11–12), 781–798.

657 Edberg, N. J. T., Wahlund, J. E., Ågren, K., Morooka, M. W., Modolo, R., Bertucci, C., &
658   Dougherty, M. K. (2010). Electron density and temperature measurements in the cold plasma
659   environment of Titan: Implications for atmospheric escape. *Geophysical Research Letters*,
660   *37*, L20105. https://doi.org/10.1029/2010GL044544

661 Edberg, N. J. T., Andrews, D. J., Shebanits, O., Ågren, K., Wahlund, J. E., Opgenoorth, H. J., et
662   al. (2013). Solar cycle modulation of Titan's ionosphere. *Journal of Geophysical Research:
663   Space Physics*, *118*(8), 5255–5264. https://doi.org/10.1002/jgra.50463

664 Fahleson, U., Fälthammar, C.-G., & Pedersen, A. (1974). Ionospheric temperature and density
665   measurements by means of spherical double probes. *Planetary and Space Science*, *22*(1), 41–
666   66. https://doi.org/10.1016/0032-0633(74)90122-6

667 Farrell, W. M., Kurth, W. S., Gurnett, D. A., Johnson, R. E., Kaiser, M. L., Wahlund, J.-E., &
668   Waite, J. H. (2009). Electron density dropout near Enceladus in the context of water-vapor
669   and water-ice. *Geophysical Research Letters*, *36*(10), L10203.

25

670   https://doi.org/10.1029/2008GL037108

671 Galand, M., Coates, A. J., Cravens, T. E., & Wahlund, J.-E. (2014). Titan's Ionosphere. In *Titan*
672   (pp. 296–361). Cambridge, UK: Cambridge University Press.

673 Garnier, P., Wahlund, J., Rosenqvist, L., Modolo, R., Agren, K., Canu, P., et al. (2009). Titan's
674   ionosphere in the magnetosheath: Cassini RPWS results during the T32 flyby. *Annales*
675   *Geophysicae*, *27*, 4257–4272.

676 Gurnett, D. A., Kurth, W. S., Kirchner, D. L., Hospodarsky, G. B., Averkamp, T. F., Zarka, P., et
677   al. (2004). The Cassini Radio and Plasma Wave Investigation. In *The Cassini-Huygens*
678   *Mission* (pp. 395–463). Springer Netherlands. https://doi.org/10.1007/978-1-4020-2774-1_6

679 Lieberman, M. A., & Lichtenberg, A. J. (2005). *Principles of Plasma Discharges and Materials*
680   *Processing: Second Edition*. *Principles of Plasma Discharges and Materials Processing:*
681   *Second Edition*. https://doi.org/10.1002/0471724254

682 Mott-Smith, H. M., & Langmuir, I. (1926). The theory of collectors in gaseous discharges.
683   *Physical Review*, *28*(4), 727–763. https://doi.org/10.1103/PhysRev.28.727

684 Mukundan, V., & Bhardwaj, A. (2018). Dayside ionosphere of Titan: Impact on calculated plasma
685   densities due to variations in the model parameters. *Icarus*, *299*, 222–239.
686   https://doi.org/10.1016/j.icarus.2017.07.022

687 Richard, M. S., Cravens, T. E., Robertson, I. P., Waite, J. H., Wahlund, J.-E., Crary, F. J., & Coates,
688   A. J. (2011). Energetics of Titan's ionosphere: Model comparisons with Cassini data. *Journal*
689   *of Geophysical Research: Space Physics*, *116*, A09310.
690   https://doi.org/10.1029/2011JA016603

691 Shebanits, O., Wahlund, J. E., Mandt, K., Ågren, K., Edberg, N. J. T., & Waite, J. H. (2013).
692   Negative ion densities in the ionosphere of Titan-Cassini RPWS/LP results. *Planetary and*
693   *Space Science*, *84*, 153–162. https://doi.org/10.1016/j.pss.2013.05.021

694 Shebanits, O., Wahlund, J.-E., Edberg, N. J. T., Crary, F. J., Wellbrock, A., Andrews, D. J., et al.
695   (2016). Ion and aerosol precursor densities in Titan's ionosphere: A multi-instrument case
696   study. *Journal of Geophysical Research: Space Physics*, *121*(10), 10,075-10,090.
697   https://doi.org/10.1002/2016JA022980

698 Shebanits, O., Vigren, E., Wahlund, J.-E., Edberg, N. J. T., Cui, J., Mandt, K. E., & Waite, J. H.
699   (2017a). Photoionization Modeling of Titan's Dayside Ionosphere. *The Astrophysical*
700   *Journal*, *850*(2), L26. https://doi.org/10.3847/2041-8213/aa998d

701 Shebanits, O., Vigren, E., Wahlund, J. E., Holmberg, M. K. G., Morooka, M., Edberg, N. J. T., et
702   al. (2017b). Titan's ionosphere: A survey of solar EUV influences. *Journal of Geophysical*
703   *Research: Space Physics*, *122*(7), 7491–7503. https://doi.org/10.1002/2017JA023987

704 Shukla, P. K., & Mamun, A. A. (2015). *Introduction to dusty plasma physics*. *Introduction to Dusty*
705   *Plasma Physics*. CRC Press. https://doi.org/10.1088/0741-3335/44/3/701

706 Vigren, E., Galand, M., Yelle, R. V., Cui, J., Wahlund, J. E., Ågren, K., et al. (2013). On the
707   thermal electron balance in Titan's sunlit upper atmosphere. *Icarus*, *223*(1), 234–251.
708   https://doi.org/10.1016/j.icarus.2012.12.010

709 Vigren, E., Galand, M., Wellbrock, A., Coates, A. J., Cui, J., Edberg, N. J. T., et al. (2016).

710 Suprathermal electrons in Titan's sunlit ionosphere: model-observation comparisons. *The*
711 *Astrophysical Journal*, *826*(2), 131. https://doi.org/10.3847/0004-637x/826/2/131

712 Vuitton, V., Yelle, R. V., Klippenstein, S. J., Hörst, S. M., & Lavvas, P. (2019). Simulating the
713 density of organic species in the atmosphere of Titan with a coupled ion-neutral
714 photochemical model. *Icarus*, *324*, 120–197. https://doi.org/10.1016/j.icarus.2018.06.013

715 Wahlström, M. K., Johansson, E., Veszelei, E., Bennich, P., Olsson, M., & Hogmark, S. (1992).
716 Improved Langmuir probe surface coatings for the Cassini satellite. *Thin Solid Films*, *220*,
717 315–320. https://doi.org/10.1016/0040-6090(92)90591-X

718 Wahlund, J. E., Boström, R., Gustafsson, G., Gurnett, D. A., Kurth, W. S., Pedersen, A., et al.
719 (2005). Cassini measurements of cold plasma in the ionosphere of Titan. *Science*, *308*(5724),
720 986–989. https://doi.org/10.1126/science.1109807

721 Wahlund, J. E., André, M., Eriksson, A. I. E., Lundberg, M., Morooka, M. W., Shafiq, M., et al.
722 (2009). Detection of dusty plasma near the E-ring of Saturn. *Planetary and Space Science*,
723 *57*(14–15), 1795–1806. https://doi.org/10.1016/j.pss.2009.03.011

724 Waite, J. H., Niemann, H., Yelle, R. V., Kasprzak, W. T., Cravens, T. E., Luhmann, J. G., et al.
725 (2005). Ion Neutral Mass Spectrometer results from the first flyby of Titan. *Science*,
726 *308*(5724), 982–986. https://doi.org/10.1126/science.1110652

727 Waite, J. H., Young, D. T., Cravens, T. E., Coates, A. J., Crary, F. J., Magee, B., & Westlake, J.
728 (2007). Planetary science: The process of tholin formation in Titan's upper atmosphere.
729 *Science*, *316*(5826), 870–875. https://doi.org/10.1126/science.1139727

730 Wang, X., Hsu, H. W., & Horányi, M. (2015). Identification of when a Langmuir probe is in the
731 sheath of a spacecraft: The effects of secondary electron emission from the probe. *Journal of*
732 *Geophysical Research: Space Physics*, *120*, 2428–2437.
733 https://doi.org/10.1002/2014JA020624

734 Wellbrock, A., Coates, A. J., Jones, G. H., Vuitton, V., Lavvas, P., Desai, R. T., & Waite, J. H.
735 (2019). Heavy negative ion growth in Titan's polar winter. *Monthly Notices of the Royal*
736 *Astronomical Society*, *490*(2), 2254–2261. https://doi.org/10.1093/mnras/stz2655

737 Whipple, E. C. J. (1965). The equilibrium electric potential of a body in the upper atmosphere and
738 in the interplanetary space. *PhD Thesis, George Washington University*.

739

740